Analysis and Augmentation of Guest-Host Interaction Energy Models as CHA and AEI Zeolite Crystallization Phase Predictors

Craig Waitt,[†] Xuyao Gao,[†] Rajamani Gounder,[‡] Anthony Debellis,[¶] Subramanian Prasad,[§] Ahmad Moini,[§] and William F. Schneider*,[†],||

†Department of Chemical and Biochemical Engineering, University of Notre Dame, Notre

Dame, IN 46556, United States

‡Charles D. Davidson School of Chemical Engineering, Purdue University, West Lafayette,

IN 47907, United States

¶Quantum Chemistry and Hybrid Modeling Research, BASF Corporation, Tarrytown, New York 10591, United States

§BASF Corporation, 25 Middlesex Essex Turnpike, Iselin, New Jersey 08830, United States

||Department of Chemistry and Biochemistry, University of Notre Dame, Notre Dame, IN
46556, United States

E-mail: wschneider@nd.edu

Abstract

The guest-host interaction energy (GHIE) is often used as a predictor of the tendency of organic structure directing agents (OSDAs) to promote the crystallization of a particular zeolite topology. Here we explore the reliability of the GHIE to predict OSDA preferences for CHA vs AEI, chosen because they have similar pore volumes, are constructed from the same secondary building units, perform similar chemistries, and are crystallized by similar OSDAs. We show that predictions are sensitive to the choice of energy model and to sampling method for some sets of OSDAs. We explore a set of secondary descriptors derived from OSDA molecular size and shape and show that a combination of GHIE and asymmetry index provides the most robust predictions.

Keywords

Zeolite, topology, crystallization, OSDA

Introduction

Zeolites are a group of crystalline, microporous polymorphs of SiO₂ that find wide practical use as catalysts, molecular sieves, and ion-exchange media. ^{1,2} Zeolite versatility is associated with their topological diversity and ability to accommodate heteroatom substitution on the Si lattice (such as Al³⁺) and associated extraframework ions. Zeolites are commonly synthesized hydrothermally in the laboratory, often with the introduction of structure directing agents to guide crystallization towards desired topologies and/or compositions. This ability has been exploited to produce zeolites optimized for a desired chemical application. ^{3–5} Alkalis are common inorganic structure directing agents, while organic structure directing agents (OSDAs) are often bulky ammonium or phosphonium cations. Given their larger size and more diffuse charge, OSDAs are often useful for creating high-silica zeolites. ^{6–10}

The size, shape, hydrophobicity, and number of charge centers on an OSDA can have a strong influence on the resulting pore dimensionality and void structure of the synthesized zeolite. Early work conducted by Gies, Marler, Zones, and Davis, explored a variety of zeolite syntheses. ^{14–17} They systematically modified the structure, size, shape, and chemical nature of template molecules, and characterized the resulting zeolite crystals. Figure 1 summarizes the role of OSDA size and shape on the observed phase crystallized. As the OSDA increases in size, but maintains its overall shape and symmetry, the void space within the zeolite also

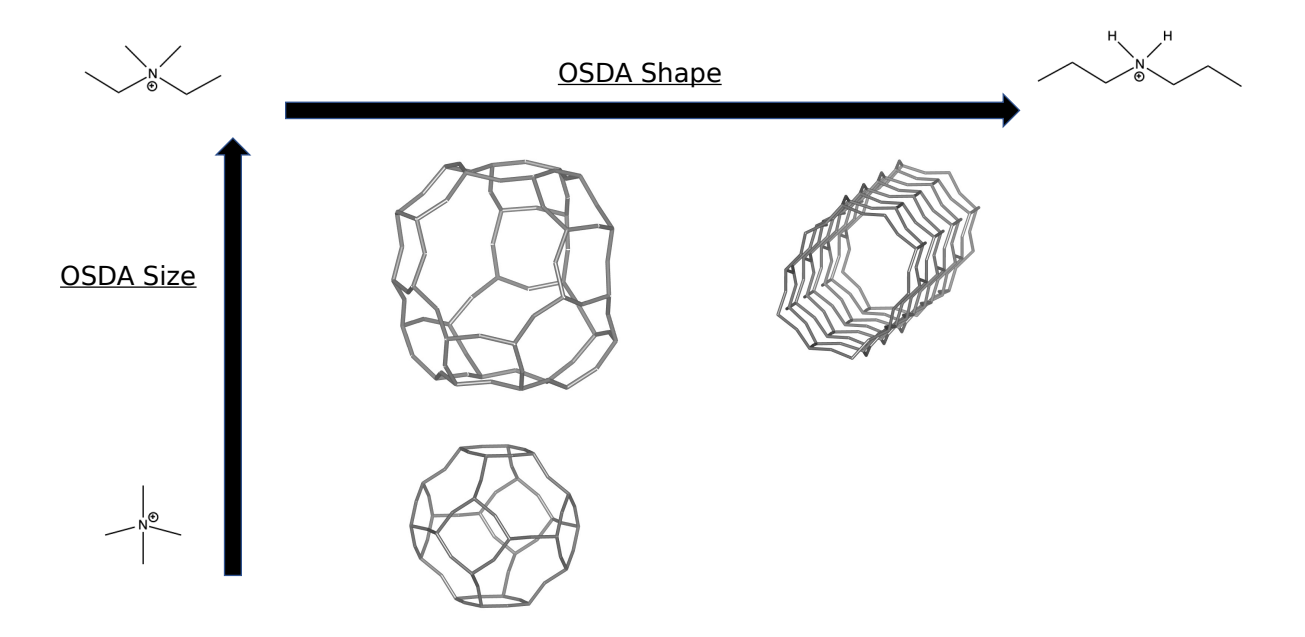


Figure 1: Pictorial representation of the influence of the OSDA size and shape on the zeolite topology crystallized. Zeolite cages and OSDAs shown belong to the SOD (lower left), ¹¹ LEV (upper left), ¹² and AEL (upper right). ¹³

increases and roughly maintains its structure and connectivity. As the OSDA becomes more asymmetric, with elongated substituents, topologies with pores and channels are formed. ^{18–23}

Computational modeling and simulations have also been employed to screen OSDAs for their ability to direct the formation of specific zeolite topologies. This approach utilizes the guest-host interaction energies (insertion energy of an OSDA into an empty zeolite void) between structure directing agents and zeolite frameworks (typically for zeolites with low Al or siliceous compositions)²⁴ as a predictor for OSDA-zeolite phase affinity. Several approaches have been proposed to evaluate the topology an OSDA prefers to crystallize.^{25–32} Recently Schwalbe-Koda et al. used classical mechanics and Monte Carlo sampling to compute the guest-host interaction energy (GHIE) of 549 known OSDAs with 209 zeolites, as well as provided structural metrics that correlate with the GHIE.³³

Chabazite (CHA) and AEI are prototypical examples of the sensitivity of zeolite products to OSDA. Both frameworks are constructed from the same double six-member ring (d6r)

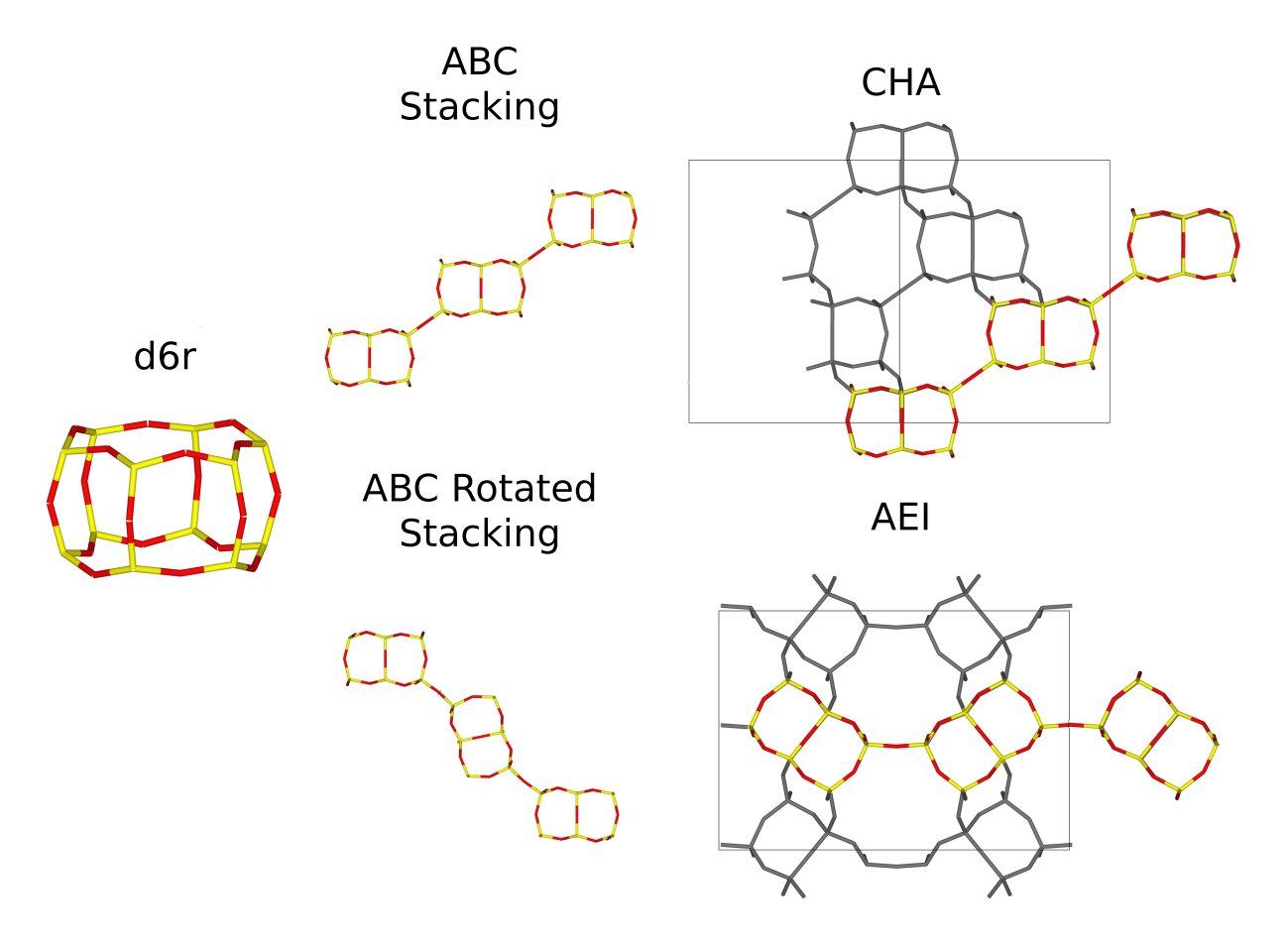


Figure 2: Representation of d6r and stacking of d6rs to form CHA and AEI topologies. Yellow and red sticks correspond to bonds between Si and O atoms.

composite building units. As shown in Figure 2, CHA is formed from d6r units stacked in an ABC pattern, creating cylindrical cages connected by 8-membered-ring (8mr) windows, while AEI is formed from the same ABC stacking, but with alternating d6rs rotated 180° to create an pear-shaped cavity. Despite their shared characteristics, such as similar synthesis protocols, ^{17,19} comparable pore volumes, and density of tetrahedral sites (T-sites), as well as their utility in similar chemical processes, ^{6,34,35} these two topologies exhibit distinct behavior in certain chemical reactions. For example, recent research by DeLuca et al. delves into the influence of zeolite cage shape and dimensionality on SCR oxidation. ³⁶ They show that CHA and AEI zeolites, despite having similar Al and Cu contents, exhibit differing rates of NO_x conversion. CHA zeolites, in particular, demonstrate rate constants nearly twice as high as

those of AEI. Consequently, the deliberate synthesis of the desired topology in CHA and AEI zeolites proves to be of paramount importance.

Although prior work has been invaluable in predicting new and useful OSDAs to prepare zeolites, there are inconsistencies regarding the phase some OSDAs prefer to crystallize, particularly for CHA and AEI zeolites. 27,33,37,38 To evaluate GHIEs, one must select a model to insert and sample a molecule within the zeolite void (most notably Monte Carlo, ³⁹ molecular dynamics, 40 or a growing methods) 25,41 and a potential model (most commonly forcefieldbased), 42-45 The combination of different potential models and sampling methods can result in discrepancies between predicted affinities toward different zeolite topologies. This motivates work to understand the implications of the choice of modeling the GHIE, as well as its use as a predictor for the OSDAs affinity to crystallize a particular framework. In this work, we compare the performance of potential models (classical forcefields and density functional theory) and sampling techniques on their influence on computed GHIEs. We select a family of trimethylammonium-based and piperidinium-based OSDAs, which are known to crystallize either CHA or AEI zeolites and apply schemes to compute the overall OSDA "fitness" (orientational landscape) of the OSDAs in the CHA and AEI voids and compare GHIEs. We show that first-principles and classical force field approaches provide similar predictions of OSDA affinities toward CHA and AEI. For cases in which there are discrepancies between GHIE and experimental observations, we show that predictions can be improved by augmenting the GHIE with simple molecular descriptors.

Computational Methods

All DFT and forcefield calculations are performed on 36-T-site CHA and 48-T-site AEI supercells using lattice parameters obtained from the Database of Zeolite Structures (IZA). ⁴⁶ Initial, isolated OSDA structures are optimized using the DFT parameters described below. Zeolite structures are in their siliceous form, and N atoms in the OSDA structures are

replaced with C (referred to as the tertiary carbon) to maintain charge neutrality. This allows us to preserve the overall size and shape of the OSDA without needing to incorporate a charge-compensating counter ion into the zeolite framework. This approach is similar to previous work completed to calculate the GHIE of charge-neutral systems. ^{26,33,38}

First-principles Calculations

Plane wave, periodic supercell DFT calculations are performed with the Vienna Ab initio Simulation Package (VASP), version 5.4.1,⁴⁷ using projector augmented wave treatment of core-valence interactions,^{48,49} and Brillouin zone sampling at the Γ-point. Energy and geometry calculations are performed using the Perdew-Becke-Ernzerhof (PBE) generalized gradient approximation⁵⁰ (GGA) with a D3, Becke-Johnson dispersion correction⁵¹ and a plane wave cutoff of 520 eV. All atoms are allowed to move during the geometry optimizations. Self-consistent field (SCF) electronic energies and forces converge to 1×10^{-5} eV and 0.01 eV/Å respectively.

Classical Molecular Dynamics Calculations

We have selected the Dreiding forcefield to evaluate the GHIEs for our classical model due to its prominent use in the literature. ^{29,32,38,52} Dreiding forcefield ⁴⁵ parameters are used to describe the self-potential of the OSDA, and van der Waals interaction between the zeolite framework and OSDA. We use molecular dynamic (MD) with constant NVT constraint using Nose-Hoover thermostat ⁵³ to sample the configurational and internal degrees of freedom of OSDAs. Si and O atoms in the zeolite frameworks are fixed in their IZA positions during MD sampling. We equilibrate the system at desired temperatures for 2000 ps, monitoring temperature fluctuations and structures to ensure that the thermostat is not introducing unphysical behavior. All MD simulations are performed within the Large-scale Atomic/Molecular Massively Parallel Simulator (LAMMPS). ⁵⁴ Example VASP and LAMMPS input files are provided in the Supporting Information (SI).

Results

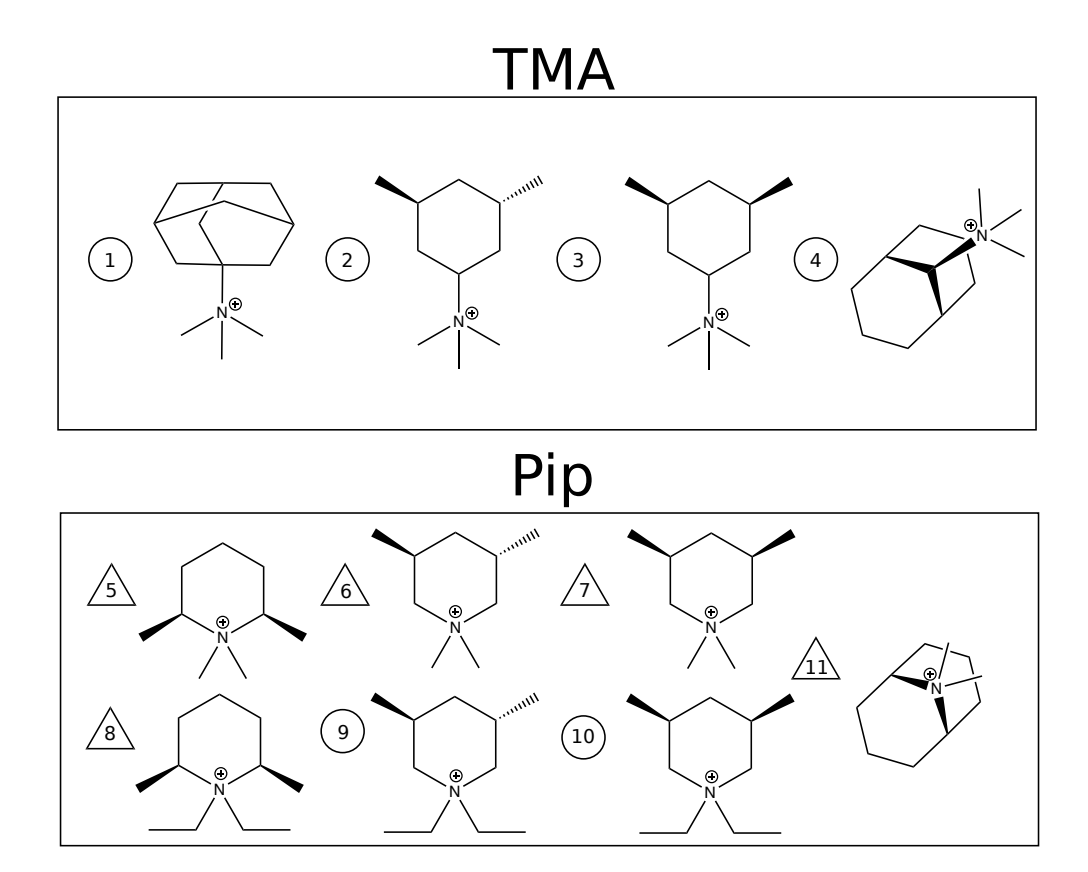


Figure 3: OSDAs separated by family. \bigcirc and \triangle correspond to OSDAs that experimentally crystallize CHA and AEI respectively. A table of OSDA IUPAC names and SMILES is provided in Table S1.

We select a family of OSDAs that are known to crystallize either CHA or AEI-type zeolites. ^{27,28,55} Figure 3 shows the 11 OSDAs of interest, separated by OSDA family. OSDAs 1-4 belong to the trimethylammonium-based (TMA) family and OSDAs 5-11 belong to the piperdinium-based (Pip) family. OSDAs 2-3, 5-7, and 8-10 are three sets of constitutional isomers or diastereomers.

Next, we compute the GHIE of each OSDA in CHA and AEI. We define the GHIE as the energy to insert a structure directing agent into the empty void of the zeolite (see equations 1 and 2). It is worth noting that the community has utilized different terminologies such as "binding energy", 32 "interaction energy", 25 "stabilization energy", 27 and "templating energy" 33 to describe the same quantity. Within the context of this problem, all of these terminologies refer to the computation of the van der Waals interactions between the OSDA and framework atoms of the zeolite. To evaluate the GHIE we insert one OSDA into the CHA and AEI cages, and sample over OSDA orientations and configurations either by discrete sampling or high-temperature 1-step annealing. In the discrete sampling approach, we generate 20 structures by randomly translating and rotating the OSDA inside the zeolite cavity. Structures are then relaxed to local minima using DFT. A new set of structures is then generated by randomly selecting a structure based on a Boltzmann distribution and randomly translating and rotating the OSDA using a "mutate" algorithm, 56 and reoptimizing this new set of structures. We repeat this procedure until a total of 50 OSDA-framework structures have been obtained. We assume these 50 structures represent the orientational landscape the OSDA can adopt within a particular framework. The GHIE ($\Delta E_{\rm GHIE}^{\rm DFT}$) of each OSDA-Framework combination is evaluated as:

$$\Delta E_{\rm GHIE}^{\rm DFT} = E_{\rm OSDA\text{-}Framework}^{\rm DFT} - E_{\rm OSDA}^{\rm DFT} - E_{\rm Framework}^{\rm DFT} \tag{1}$$

where $E_{\text{OSDA-Framework}}^{\text{DFT}}$, $E_{\text{OSDA}}^{\text{DFT}}$, and $E_{\text{Framework}}^{\text{DFT}}$ are the energies of the 50 structures, isolated OSDA, and empty siliceous framework respectively.

In the high-temperature 1-step annealing approach, we perform classical MD simulations at 5000 K for 2000 ps with a 0.2 fs time step. We use the first 1000 ps as an equilibration run and the last 1000 ps as a production run. We identify the accessible orientations the OSDA explored by binning the structures into eight sections based on the angle the tertiary carbon makes with a principal axis of the zeolite cage (see Figure 4). We resample the eight different low-energy orientations at 343 K in the same manner as described in the 5000 K simulation above. We first equilibrate the system for 1000 ps followed by a 1000 ps production run. We

calculate the GHIE ($\Delta E_{\mathrm{GHIE}}^{\mathrm{CMD}}$) of each of the eight trajectories as:

$$\left\langle \Delta E_{\text{GHIE}}^{\text{CMD}} \right\rangle = \left\langle E_{\text{OSDA-Framework}}^{\text{CMD}} \right\rangle - \left\langle E_{\text{OSDA}}^{\text{CMD}} \right\rangle - E_{\text{Framework}}^{\text{CMD}}$$
 (2)

Isolated OSDA energies are calculated from DFT and classical simulations with one OSDA molecule placed in a $20 \times 20 \times 20$ Å³ box. For the CMD calculations, the average OSDA energy at 343 K is used. A link to all the structures is provided in the SI. We normalize our final energies based on the number of T-sites per CHA and AEI cage (12). While we had the option to normalize our final energies by the number of OSDAs, for the purposes of this study, this choice does not impact our final observations and conclusions. Nevertheless, when comparing the GHIEs of zeolite topologies that contain varying numbers of organic molecules within the zeolite voids, it is crucial to exercise caution and ensure that proper comparisons are made.

OSDA Orientational Landscape

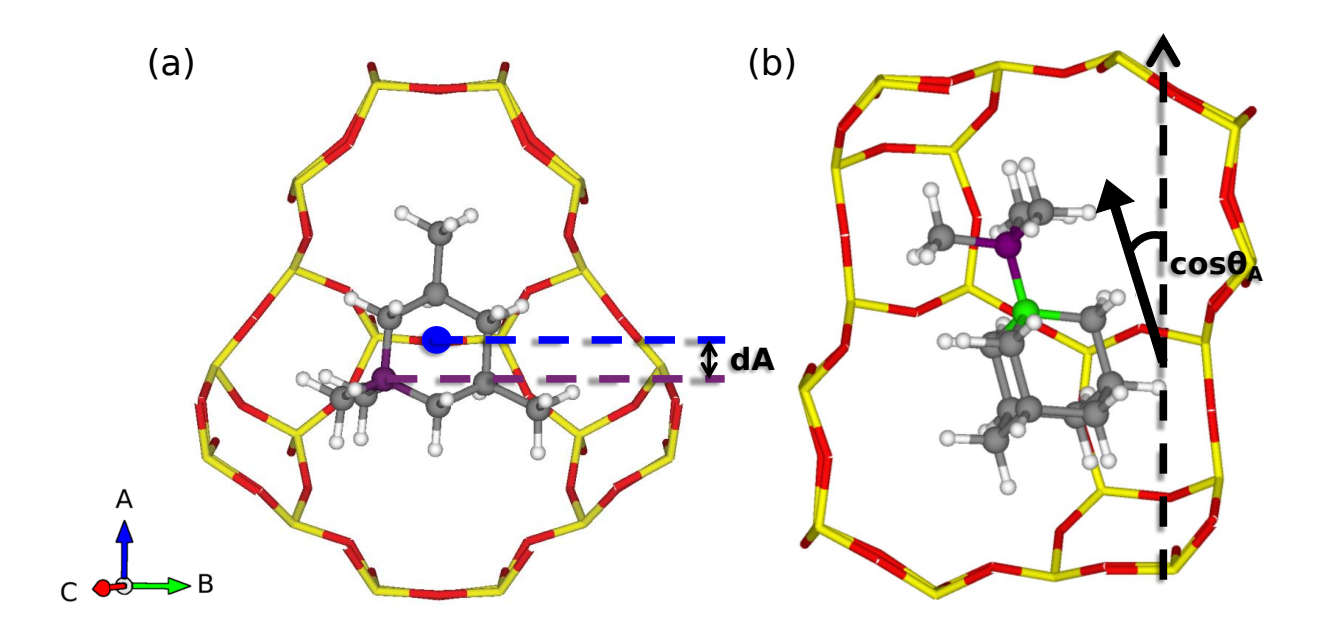


Figure 4: Schematic illustration of translational and orientational descriptors. (a) Translational displacement of the tertiary carbon (purple) from the center of zeolite void (blue) along the three principal axes. (b) Cosine angle between OSDA internal vector from the tertiary carbon to an adjacent carbon (green) and the three principal axes.

To describe the orientational landscapes available to OSDAs within the two frameworks, we define three translational descriptors of the OSDA tertiary carbon from the center-of-mass of the cage along each of the three principal axes, labeled A, B, and C to indicate the long axis (A) and two orthogonal short axes (B and C) of the supercells. These descriptors report on displacement towards a particular area of the cage (e.g. the bottom or top of a cage). We similarly define three orientational descriptors as the cosines of the angles between an OSDA orientation vector, taken to be a vector from the tertiary carbon to an adjacent or cross-ring carbon, and each of the three principal axes (Figure 4). Negative, zero, and positive values correspond to antiparallel, orthogonal, and parallel orientations relative to the principal axis.

We compare the behaviors of OSDAs 1 and 8, which have strong affinities towards CHA and AEI respectively, ^{27,28} as representative of the TMA and Pip families, respectively, in CHA and AEI. Figures 5, 6, report the displacement and orientational parameters and GHIE for all 50 structures from the discrete sampling method. All other OSDA-framework combinations, and results from the high-temperature 1-Step annealing approach, are reported in Figures S1-S20.

To extract parameters from the molecular dynamics trajectories (high-temperature 1-step annealing method), we initialize the OSDA in the void such that the cosine between the OSDA vector and the A-axis is -1, then run molecular dynamics at 5000 K. We note that certain OSDAs depicted in Figure 3 exhibit stereoisomeric relationships, specifically, OSDAs 6-7 and 9-10. At these elevated temperatures, there exists the possibility of interconversion between these stereoisomeric states among the OSDAs. To address this potential phenomenon, we monitor the chirality of these OSDAs by measuring the dihedral angles of the methyl substituents. Structures that undergo interconversion between cis and trans isomeric configurations are removed from the trajectory (approximately 10% of the entire trajectory). Then we bin the 5000 K trajectories into eight equal sections based on the OSDA orientation along the asymmetric axis of the CHA and AEI cages (A-axis), select the

lowest energy structure from each region, and resample the configurations at 343 K using the parameters described in the methods section (Figures S21-S42). From these eight trajectories, we extract the average and standard deviation of potential energy, three translational descriptors, and three orientational descriptors, which are reported in Figures S10-S20. Representative low energy orientations for each OSDA-Zeolite combination are shown in Figures S43-S53.

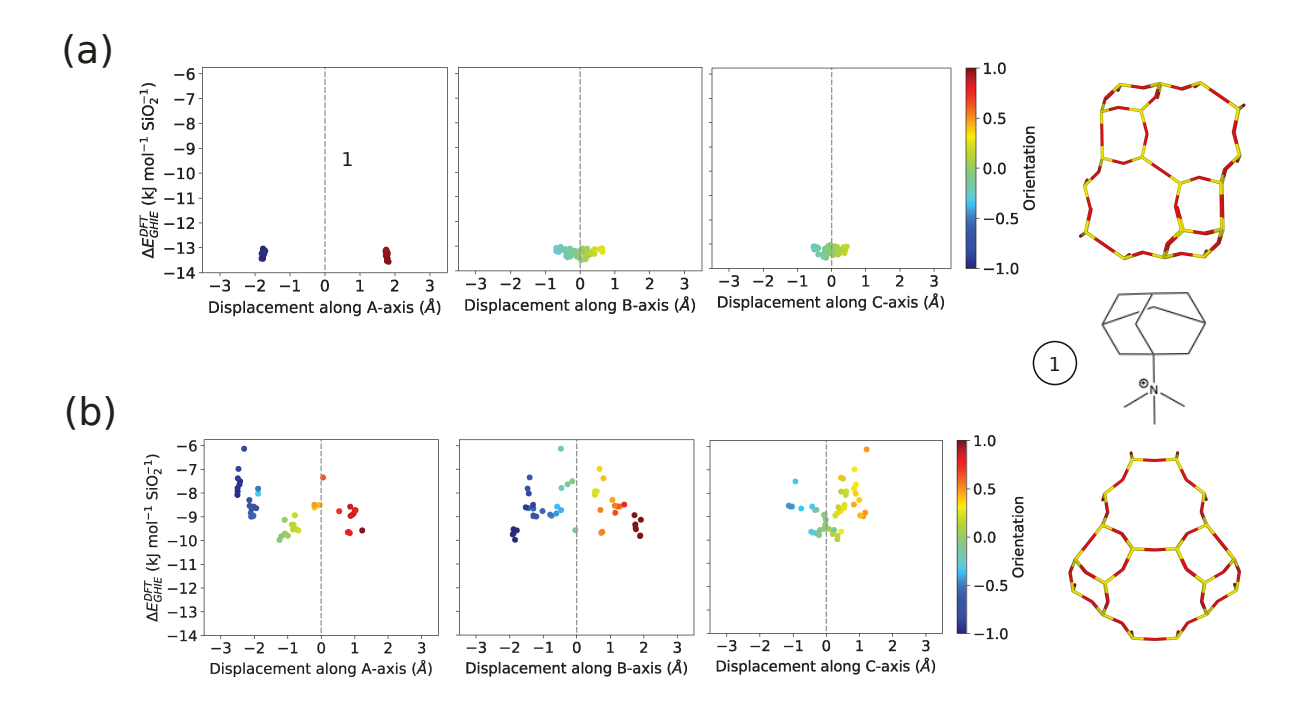


Figure 5: Orientational landscapes of OSDA 1 in (a) CHA and (b) AEI as extracted from the discrete sampling method.

Figure 5(a) reports results for OSDA 1 in CHA, plotted as displacements with respect to the three principal axes along the x-axis, GHIE along the y-axis, and color-coded by orientations. The orientation and displacement along the A(long)-axis show two clusters of points centered about -2 and 2 Å, with isoenergetic orientation values of -1 and 1 respectively. These clusters correspond to the tertiary carbon pointing parallel (as depicted in Figure S43(a)) and antiparallel to the A axis. In the initial generation of structures, two configurations with the OSDA orthogonal to the A axis were created, but when relaxed to a local minimum, had positive interaction energies (> 100 kJ mol⁻¹), which suggests that

the OSDA does not orient in the CHA cage perpendicular to the A axis and is consistent with previously reported results of OSDA 1.52,57,58 The energy distribution of each cluster of points varies about $0.6 \text{ kJ mol}^{-1} \text{ SiO}_2^{-1}$. The orientations along the B and C axes are centered at 0 Å and range in value from -0.25 to +0.25, which corresponds to the OSDA being centered in the middle of the cage. These plots show that OSDA 1 is confined to one of two orientations in the CHA cage, parallel or antiparallel to the A-axis. The other TMA OSDAs in CHA (Figures S1-S3) similarly cluster into parallel and antiparallel orientations along the A-axis, but GHIE values are somewhat less negative.

Figure 5(b) reports results for OSDA 1 in AEI. Unlike CHA, the OSDA is able to access a broad envelope of orientations, with three distinct clusters orthogonal (as depicted in Figure S43(c)), parallel, and antiparallel to the A-axis. The orthogonal orientation is lowest in energy, followed by parallel and then antiparallel. The antiparallel configuration places the bulky end of the OSDA into the narrow end of the AEI cage, raising the energy. The GHIEs between low and high energy orientations vary by 4 kJ mol⁻¹ SiO₂⁻¹ and are less negative than OSDA 1 in CHA. As shown in Figures S1-S3 and S10-S13, the other TMA OSDAs behave similarly in AEI.

Observations from analysis of the high-temperature 1-step annealing method also show that the OSDAs are confined to a parallel or antiparallel orientation in the CHA void, and exhibit a broad range of orientations in AEI. Figures S21-S28 show upon quenching the simulation at 343 K, the OSDA orientations collapse toward -1 in CHA (as depicted in Figure S43(b)-S46(b)). We do not observe OSDA orientations at +1 in the high-temperature 1-step annealing approach because the TMA OSDAs are sterically hindered to rotate. GHIE are considerably more exothermic than the discrete sampling method (-6 kJ mol $^{-1}$ SiO $_2$ ⁻¹ for OSDA 1 and -2 kJ mol $^{-1}$ SiO $_2$ ⁻¹ for OSDA 4). This difference can be rationalized by comparing differences in GHIEs attributed to the different potential models and sampling methods. A detailed comparison is presented on page S61 of the SI. We believe the discrepancy between these GHIEs, is primarily attributed to the inherent differences in the DFT

and Dreiding forcefeild calculations.

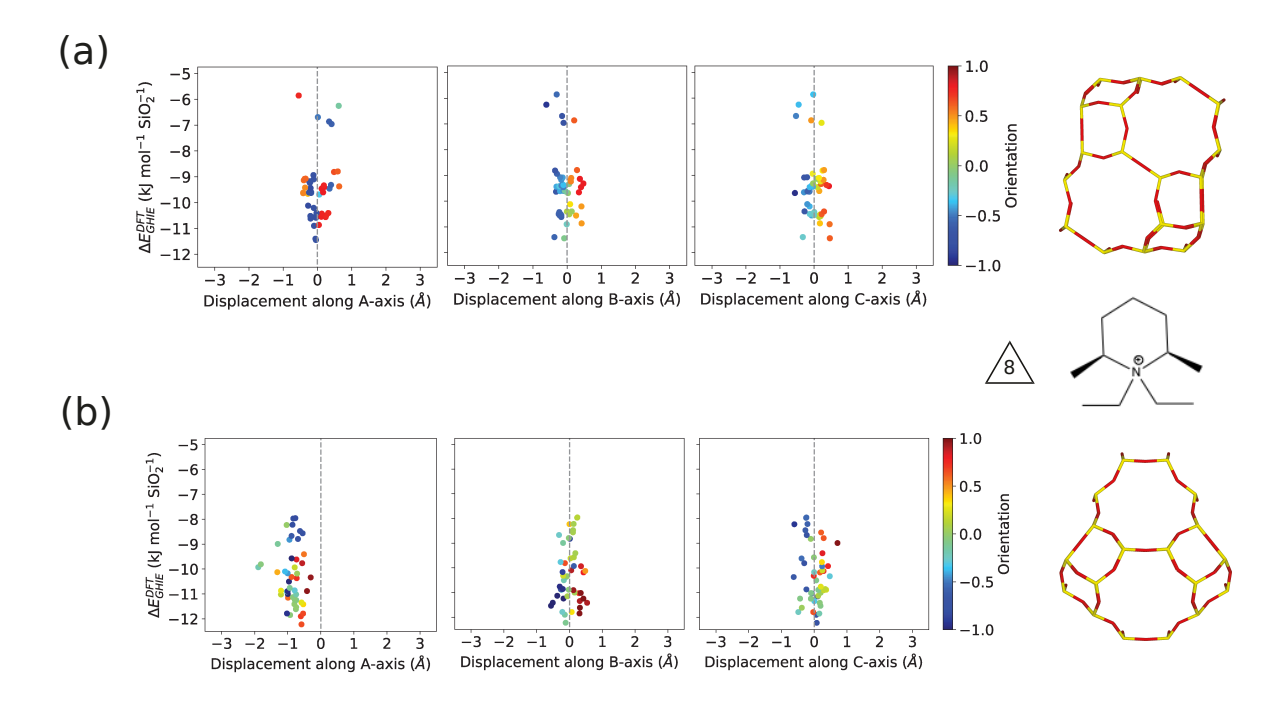


Figure 6: Orientational landscape of OSDA 8 in (a) CHA and (b) AEI as extracted from the discrete sampling method.

Figures 6(a) and (b) plot the orientations of OSDA 8 in CHA and AEI respectively, extracted from the discrete sampling method. In contrast to the TMA OSDA (Figure 5), the Pip OSDA can access a broader range of orientations inside the voids of both CHA and AEI. As shown in Figure 6(a), OSDA 8 can adopt several isoenergetic orientations within the CHA void. The lowest energy orientations are those in which the tertiary carbon is located near the center of the CHA cage and the OSDA is pointing parallel or antiparallel to the A-axis, similar to the TMA OSDAs. We observe one metastable configuration at $-6 \text{ kJ mol}^{-1} \text{ SiO}_2^{-1}$, where the OSDA is oriented orthogonally to the A-axis. As shown in Figure 6(b), OSDA 8 behaves similarly in AEI, with the exception that the tertiary carbon is confined to the wide end of the AEI void (-1 Å) and the center-of-mass of the OSDA prefers to avoid the narrow end of the cage. Pip OSDAs 5-7 and 11 behave similarly in CHA and AEI (Figures S4-S6 and S9).

The Pip OSDAs 9 and 10 exhibit distinct behavior. Figure 7 reports orientational de-

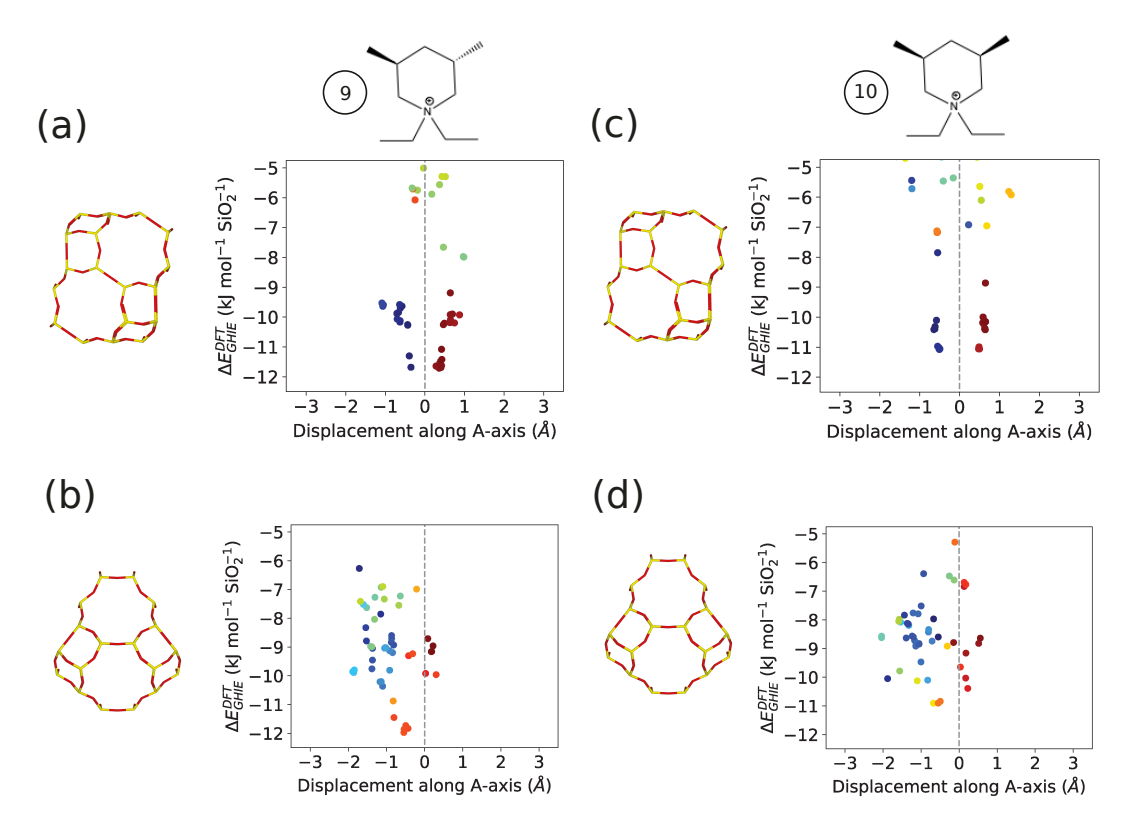


Figure 7: Orientational landscape of OSDA 9 in (a) CHA and (b) AEI and OSDA 10 in (c) CHA and (d) AEI along the A-axis, as extracted from the discrete sampling method.

scriptors along the A-axis of each OSDA in CHA and AEI (full landscape shown in Figures S7 and S8). Results resemble the TMA- more than the Pip-family, in particular, two clusters of low energy-oriented parallel and antiparallel to the A-axis and centered in the BC plane in CHA, and a broad envelope of orientations in AEI (as in Figures S1-S3). The high-temperature 1-step annealing method also shows that these OSDAs are conformationally rigid in the CHA void and do not explore "flipped" configurations like other Pip OSDAs in CHA (Figures S10-S20 and S21-S42).

Three general observations can be drawn from these comparisons. First, the choice of utilizing DFT with a discrete sampling method and Dreiding forcefield with high-temperature 1-step annealing produces similar low-energy OSDA configurations. The approaches we have taken here highlight the complicated and nuanced challenges encountered when attempting to determine the affinity of an OSDA towards a specific zeolite topology. The results thus demonstrate that the combination of a robust sampling method and satisfactory potential model are sufficient to explore OSDA orientation space and determine GHIEs. Second, we observed that TMA OSDAs in CHA can access the entire cage and are limited to parallel and antiparallel orientations with respect to the A-axis. In AEI, the TMA OSDA center of mass is confined to the wide end of the cage, resulting in GHIEs that are less negative than in CHA. Third, with the exception of OSDAs 9 and 10, the GHIEs for the Pip OSDAs are more negative in AEI than in CHA. They are confined to the wide end of the AEI cage but can access a broad envelope of orientations. It remains unclear why OSDAs 9 and 10 behave similarly to the TMA OSDAs.

OSDA Phase Affinity for CHA and AEI

To evaluate the tendency to crystallize CHA vs AEI, we identify the lowest energy configuration from each sampling method for each OSDA-framework combination and compute

 $\Delta\Delta E_{\rm GHIE}$ as the difference between the CHA and AEI GHIE:

$$\Delta \Delta E_{\text{GHIE}} = \Delta E_{\text{GHIE}}^{\text{CHA}} - \Delta E_{\text{GHIE}}^{\text{AEI}}$$
 (3)

Figure 8(a) reports $\Delta\Delta E_{\rm GHIE}$ from the discrete sampling method, and Figure 8(b) similarly for the high-temperature annealing. OSDAs are sorted from lowest to highest energy in Figure 8(a), and is consistent for the subsequent figures. For comparison, we include results reported in the OSDB (Organic Structure-directing agent DataBase), ³³ which uses Dreiding force field parameters combined with Voronoi docking ³⁹ to sample the OSDA orientational space, in Figure 8(c).

Figure 8 (a) plots the $\Delta\Delta E_{\rm GHIE}$ from the DFT/discrete sampling method for the OSDAs presented in Figures S43(a)-S53(a) and S43(c)-S53(c). The TMA OSDAs (1-4) all have a strong preference for CHA over AEI, with OSDA 1 having the strongest affinity for CHA $(-3.6~{\rm kJ~mol^{-1}~SiO_2^{-1}})$ and OSDA 4 being the weakest $(-1.2~{\rm kJ~mol^{-1}~SiO_2^{-1}})$. The GHIE model predicts that these OSDAs will crystallize CHA zeolites, which aligns with experimental observations. Pip OSDAs (5-11) have a slight preference for AEI (relative to the TMA OSDAs preference toward CHA) or equal preference for CHA and AEI. OSDA 5 has the strongest affinity toward AEI (1.5 kJ $\mathrm{mol}^{-1}~\mathrm{SiO_2}^{-1}$) and OSDA 9 is the weakest $(0.3 \text{ kJ mol}^{-1} \text{ SiO}_2^{-1})$. OSDA 10 is the only Pip OSDA where the GHIE model predicts crystallization of the CHA phase $(-0.2~\mathrm{kJ~mol^{-1}~SiO_2^{-1}})$. OSDAs 5-8 and 11 are known to experimentally crystallize AEI zeolites, whereas OSDAs 9 and 10 crystallize CHA. The GHIE model predictions mostly agree with experimental observations with the exception of OSDA 9. This discrepancy in GHIE for OSDAs 9 was also observed in an earlier study. ²⁷ We note that OSDAs 9-10 are diastereomers. While we are unaware of any report in which a pair of diastereomers crystallize different zeolite topologies, it is known that mixtures of stereoisomers can have an impact on the rate of crystallization as well as composition.⁵⁹

Figures 8(b) and 8(c) plot the $\Delta\Delta E_{\rm GHIE}$ from our Dreiding/high-temperature 1-step

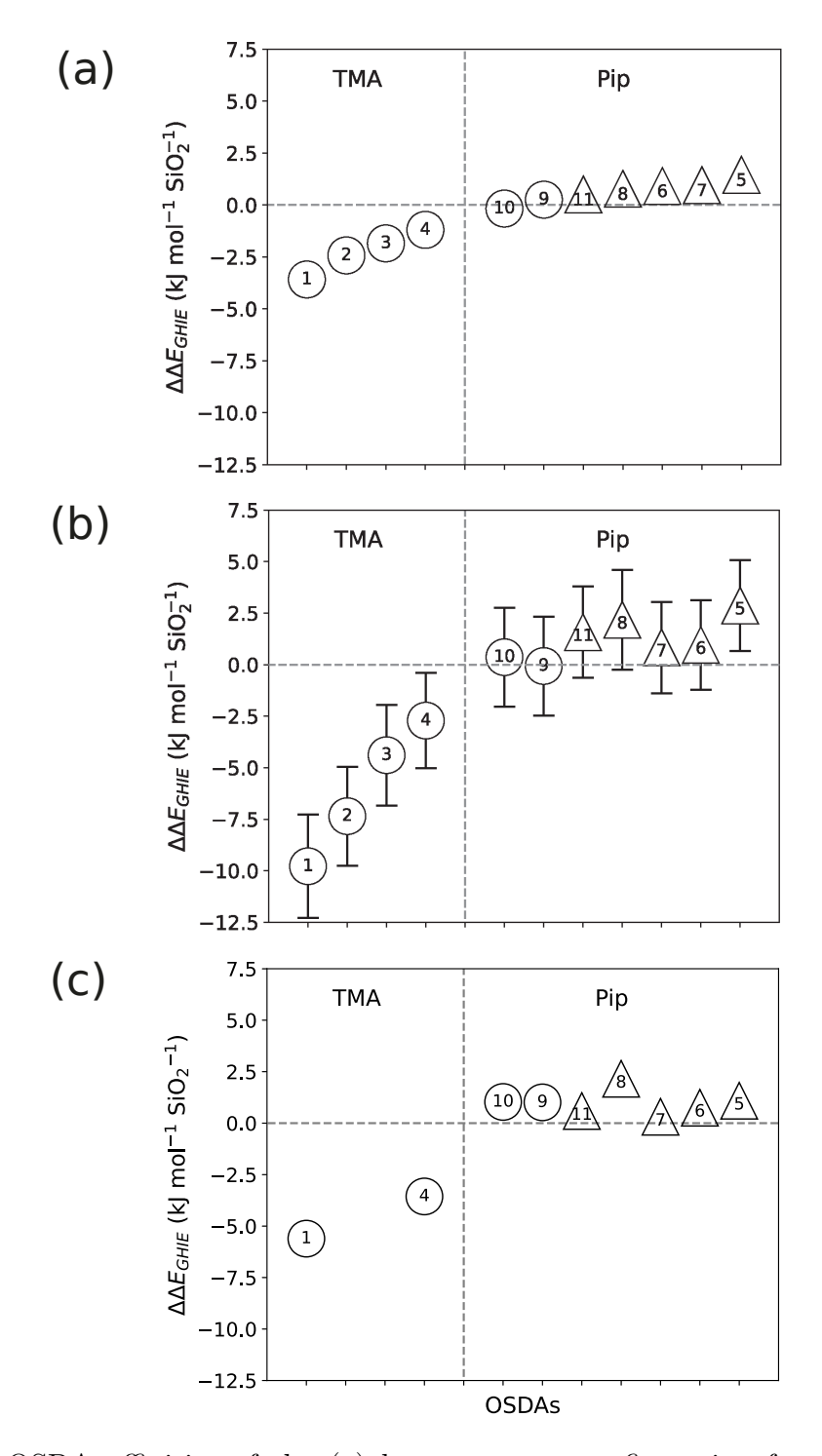


Figure 8: OSDA affinities of the (a) lowest energy configuration from the discrete sampling technique, (b) lowest average energy from high-temperature 1-step annealing, and (c) configurations reported in the OSDB. \bigcirc and \triangle correspond to OSDAs that experimentally crystallize CHA and AEI respectively. Table S2 contains the data presented in Figure 8.

annealing method and the OSDB (OSDAs 2 and 3 are not reported in the OSDB). Both show trends similar to those reported in Figure 8(a). The predictions made for OSDAs 1-8 and 11 are consistent with experimental observations. In Figure 8(b), it is evident that OSDA 5 emerges as the most favored among the OSDAs for AEI, with OSDA 8 following closely. In Figure 8(c), conversely, we observe the opposite. The energies reported in Figure 8(c) are extracted from the OSDB, normalized by the SiO_2 subunit. When we examine the structure of OSDA 8 in AEI, only three of the four zeolite voids are occupied by the structure-directing agent, leaving the fourth void empty. The reported GHIE per SiO_2 for OSDA 8 in CHA is predicted to be significantly more favorable than in AEI. To make a fair comparison with OSDA 8 in the CHA model, we use the GHIE normalized by OSDA, multiply it by a factor of 4 to simulate a fully occupied zeolite, and then normalized by the number of T-sites/cage (12). This adjustment may account for the observed shift in trends between Figures 8(b) and 8(c) but predicts the correct phase OSDA 8 will crystallize. For comprehensive details of all GHIEs used in the computation of $\Delta\Delta E_{GHIE}$, see Table S2.

Figure 8(b) shows that the standard deviations of most of the Pip OSDAs fall into the CHA regime. Additionally, the phases predicted by OSDAs 9 and 10 vary across the three sampling methods. The discrete sampling method predicts OSDA 9 will crystallize AEI whereas OSDA 10 will crystallize CHA. The high-temperature 1-step annealing method predicts OSDA 10 will crystallize AEI and OSDA 9 will crystallize CHA (with standard deviations reaching into the CHA/AEI regimes). The Voroni docking results from the OSDB predict both to crystallize AEI. OSDAs 9 and 10 have a similar orientational landscape as the TMA OSDAs, which may be attributed to the size and distribution of substituents on the molecule. This suggests that there is a "fitness" component to structure directing associated between the molecular shape and size of the OSDA and the shape of the CHA and AEI cavities.

Augmentation of GHIE Descriptor

Fitness descriptors other than GHIE have been used to relate OSDA shape to zeolite crystal-lization patterns. For example, Zones et al. compared the affinity of 11 piperidinium-based OSDAs in CHA and AEI, and observed a correlation between the total number of C and N atoms with the OSDAs directivity towards a particular topology. Thowever, the influence of the shape of OSDAs is not captured and is not easily extendable to other types of OSDAs. Earlier work has explored the influence of shape-based descriptors in order to obtain more faithful predcitions of an OSDAs affinity toward ITE zeolites. Here we explore the performance of a set of easily computable, "simple" descriptors that capture the general size and shape of OSDAs to see if crystallization patterns emerge.

We quantify the OSDA molecular size using the number of carbon atoms and the molecular van der Waals volumes. Figures 9(a) and (b) plot the $\Delta\Delta E_{\rm GHIE}$ from Figure 8(a), as a function of each of these descriptors respectively. We find that smaller OSDAs (< 12 C atoms and < 205 Å³) have a stronger tendency to prefer AEI, while larger OSDAs (> 12 C atoms and > 205 Å³) prefer CHA. However, at 12 C atoms and 205 Å³, we do not see any clear trends to crystallize one topology over another. OSDA 2, 3, and 8-10 all have relatively the same molecular size, yet crystallize different topologies. These observations are commensurate with previously reported results. ^{27,28,33,55} Thus, OSDA size is not an appropriate descriptor to resolve the discrepancies in predicted GHIEs for CHA and AEI.

To quantify molecular shape, we use descriptors that capture the distribution of substituents on the molecule: molecular eccentricity and asymmetry index. Molecular eccentricity (ζ) , ⁶¹ which measures how elliptical or circular a molecule is, is defined as:

$$\zeta = \frac{\sqrt{I_a^2 - I_c^2}}{I_a} \tag{4}$$

where I_a and I_c are the largest and smallest moments of inertia of the OSDA and range from 0 (circular) to 1 (elliptical). The asymmetry index $(\kappa)^{62}$ measures how prolated or oblated

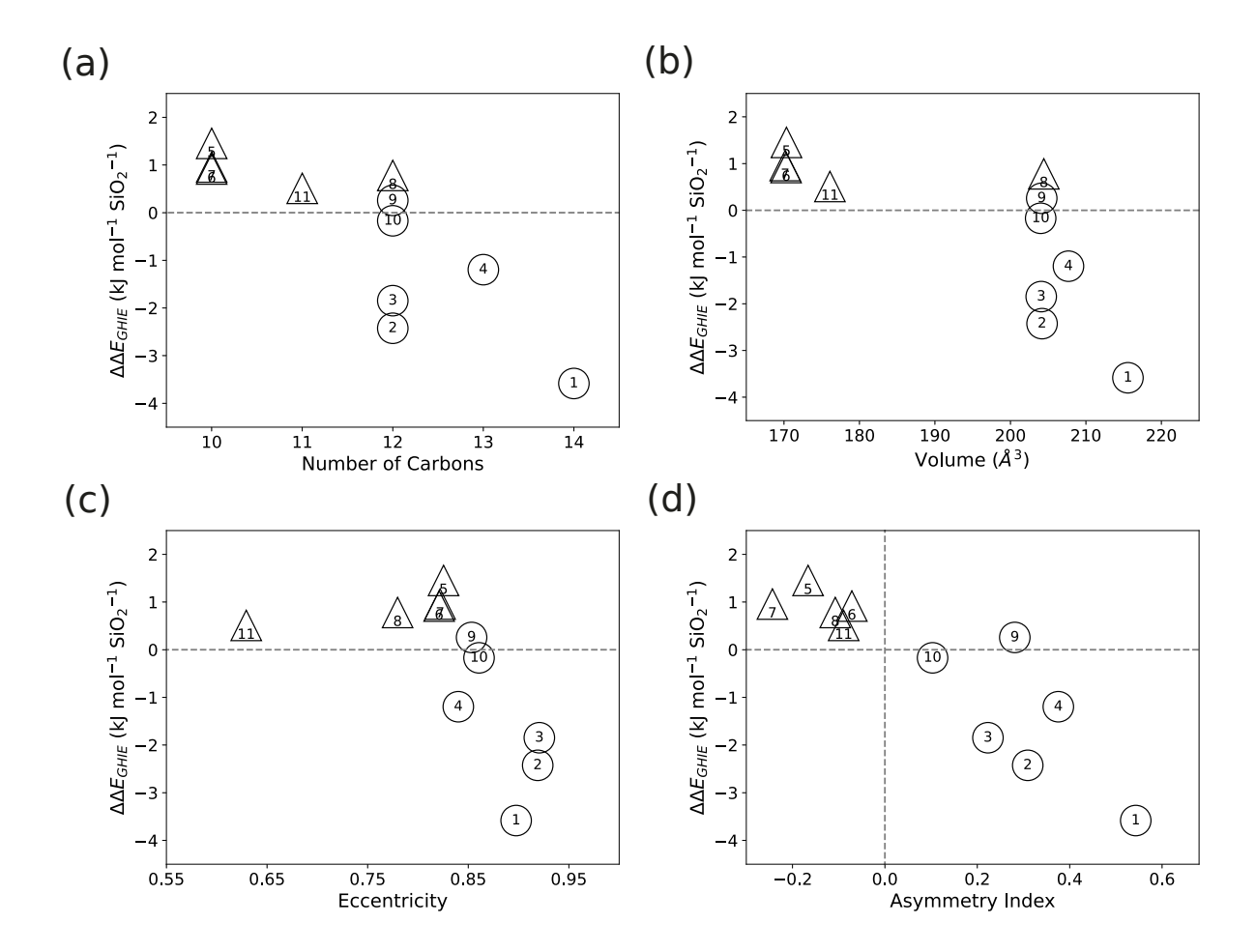


Figure 9: Comparison of (a) number of carbons per OSDA, (b) molecular volume, (c) molecular eccentricity, and (d) asymmetry index with respect to predicted phase affinity. \bigcirc and \triangle correspond to OSDAs that experimentally crystallize CHA and AEI respectively. The vertical dashed line in Figure 9 (d) corresponds to a molecule with equal principal moments of inertia.

a molecule is and is defined as:

$$\kappa = \frac{I_c}{I_b} - \frac{I_b}{I_a} \tag{5}$$

which ranges from -1 (plate-shaped) to +1 (rod-shape). We calculate the OSDA moments of inertia for each descriptor by averaging the moments of inertia from MD simulation of gas phase OSDAs. The standard deviation of the moments of inertia are relatively small, suggesting the bulk of the OSDA molecules are rigid and the substituent flexibility has a small effect on the overall moments of inertia. MD is performed with Dreiding forcefield at 600 K for 2000 ps with 0.2 fs timestep.

Figures 9(c) and (d) plot the $\Delta\Delta E_{\rm GHIE}$ as a function of each of these two descriptors. For our set of OSDAs, we find that when we use the eccentricity descriptor, we begin to see a separation of OSDAs at about 0.85. Those OSDAs above 0.85 have a more elongated shape and predict the crystallization of CHA. Those below 0.85 are more circular and predict the crystallization of AEI. OSDAs 9 and 10 predict different preferred topologies but have eccentricity values commensurate with other TMA OSDAs. When using the asymmetry index, we find that all OSDAs that experimentally crystallize CHA have positive asymmetry indices and negative $\Delta \Delta E_{\text{GHIE}}$ (except for OSDA 9 which is only slightly positive) while those that crystallize AEI have negative asymmetry indices and positive $\Delta\Delta E_{\rm GHIE}$. We observe a clear and distinct separation of CHA-favored and AEI-favored OSDAs. The asymmetry index resolves the difference in the distribution of substituents particularly for isomers 2-3, 5-7, and 8-10. Our augmented scheme has the characteristics of being able to correctly predict the phase preference an OSDA will crystallize; OSDAs that are cylindrical will tend to favor the cylindrical CHA, whereas more oblate molecules will prefer to crystallize the pear-shaped AEI cage. The computation of the asymmetry index is also not sensitive to the mode used to compute GHIEs and therefore could be considered as a secondary descriptor to predict the affinity of an OSDA towards CHA or AEI.

Discussion

Based on the results shown in Figure 9, we observe a strong correlation between the asymmetry index, GHIEs, and affinity for the OSDA to crystallize either CHA or AEI. This new scheme can be utilized to aid in determining whether an OSDA prefers to crystallize one of these two zeolite topologies. As a test, we apply our descriptor model to the entire set of TMA and Pip OSDAs in the OSDB.

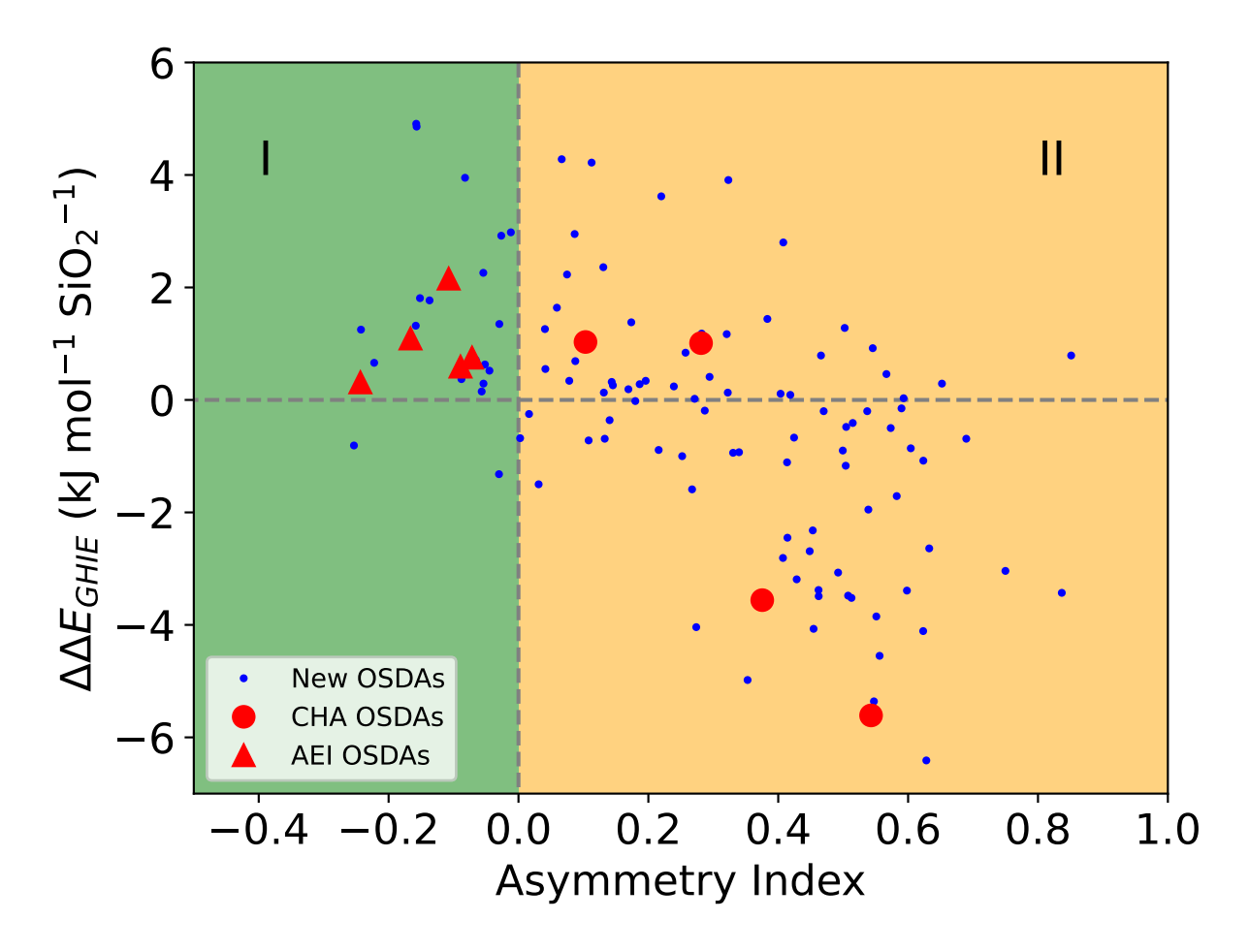


Figure 10: Comparison of asymmetry index with respect to predicted phase affinity for TMA and Pip OSDAs from the OSDB. Red points correspond to the OSDAs in Figure 8(c). Blue points correspond to new TMA and Pip (structures in the SI). Different regions are highlighted in green and orange.

Figure 10 plots 102 new TMA and Pip OSDAs that resemble OSDAs in the TMA or Pip family, and their asymmetry indices (blue), as well as the nine original OSDA from Figure

8(c) (red). We obtain the OSDAs moments of inertia by selecting one OSDA in a CHA cage and delete all other atoms. We use the moments of inertia of these static structures to compute the asymmetry indices (see Table S3). We observe similar trends between the nine OSDAs in Figure 10 and Figure 9(d). The OSDAs in these two plots have the same asymmetry index and different values of $\Delta\Delta E_{\rm GHIE}$. For the other 102 OSDAs (most of which have not previously been shown to crystallize CHA or AEI), we find that about 80% of the structures fall into regime II (with positive asymmetry indices) and 20% of the structures fall in regime I (with negative asymmetry indices). This large distribution of OSDAs in regime II may suggest why AEI cannot be made as robustly as CHA. There are fewer OSDAs that are appropriately shaped to be accommodated in the AEI voids as compared to CHA. We note that our model does not account for configurational changes an OSDA can adopt to be occluded in the zeolite cage. Some templating molecules can fold and contort to fit within the zeolite voids, which impacts the final asymmetry index and introduces strain energy in the OSDA. This is particularly evident when comparing OSDAs in regime II that have large positive $\Delta\Delta E_{\rm GHIE}$ and positive asymmetry indices.

This augmented methodology for determining the directivity of OSDAs towards CHA or AEI zeolites can also be employed to identify novel potential candidates for crystalizing CHA or AEI. Figure 11(a) and (b) plots the $\Delta E_{\rm GHIE}$ vs. asymmetry index for the OSDAs presented in Figure 10 in CHA and AEI respectively. By utilizing this applied methodology, we can now identify OSDAs that exhibit comparable $\Delta E_{\rm GHIE}$ and asymmetry indexes, enabling the prediction of new OSDA candidates. For instance, the candidate highlighted in Figure 11(a) belongs to the "spiro" family, which has been explored as candidates for crystallizing CHA. ^{19,33} Depending on synthesis details, this specific candidate has been used successfully to crystallize CHA as well as BEA, CON ¹⁷ and MWW. ⁶³ Conversely, when examining available OSDAs with a comparable affinity for AEI as OSDA 8, we find no other OSDA families that can crystallize AEI as effectively. OSDA 8 has previously proven its ability to crystallize AEI zeolites under various synthesis conditions. ^{19,55} This is unsurpris-

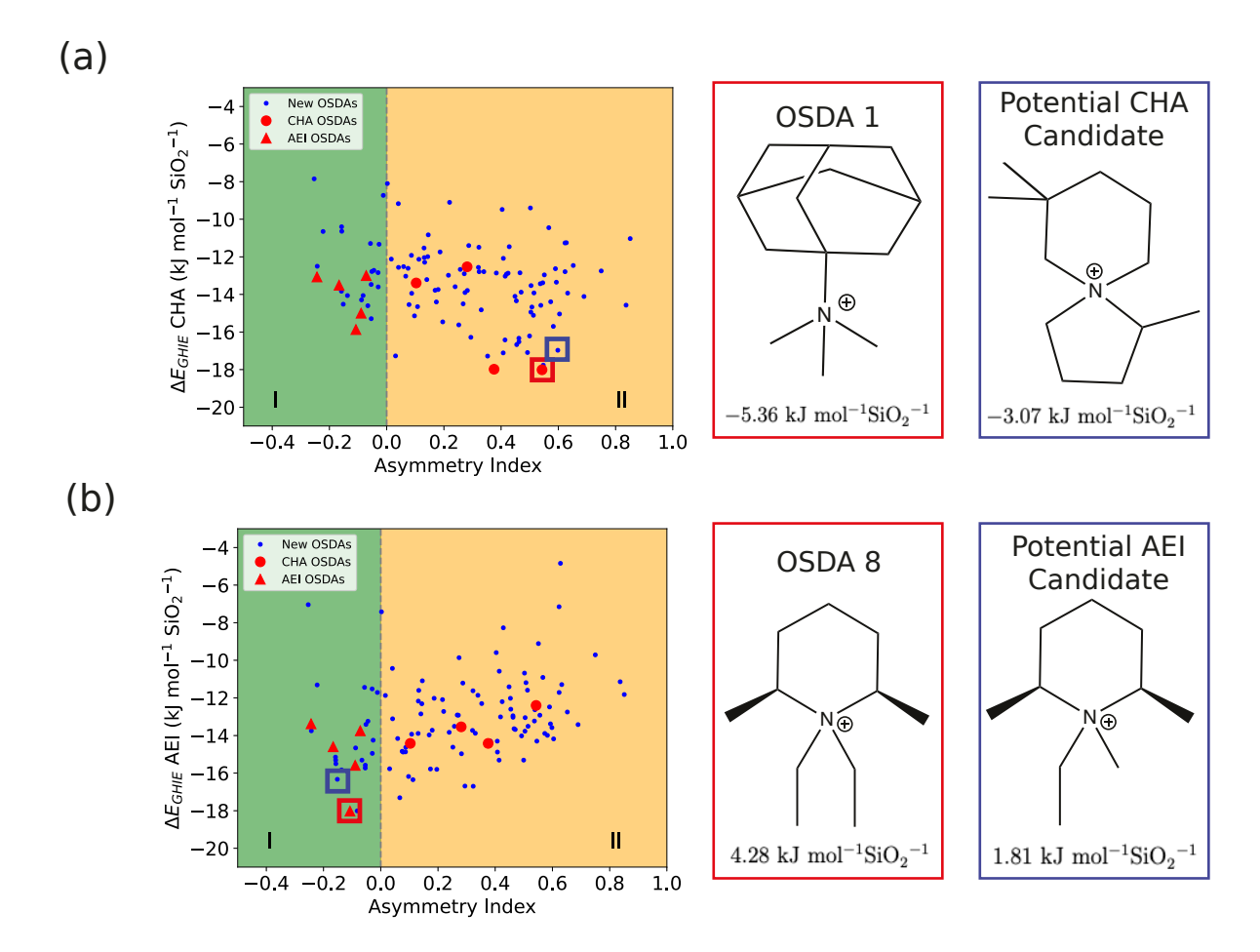


Figure 11: $\Delta E_{\rm GHIE}$ of OSDAs from the OSDB in (a) CHA and (b) AEI. Red points correspond to OSDAs in Figure 8(c). Blue points correspond to new TMA and Pip (structures in the SI). OSDAs with the strongest $\Delta E_{\rm GHIE}$ and potential new OSDA candidates are highlighted in red and blue boxes respectively. Computed $\Delta \Delta E_{\rm GHIE}$ are shown to highlight the OSDA affinities toward CHA and AEI.

ing as AEI syntheses are less diverse than CHA as previously reported. ⁶ It should be noted that our model neglects the potential influence of co-cations (such as Na⁺, F⁻, or co-SDAs) which can have an influence on the accessible orientations a structure directing agent can adopt within the zeolite pores. Depending on the distance between the charged ends of structure directing agents or the steric effect of occupying multiple species in one cage an appreciable effect could arise which might contribute to favoring or disfavoring certain OSDA orientations, potentially affecting phase selectivity. ³⁰ Additionally, our model neglects the role of OSDA-OSDA interactions across two adjacent cages which can have a similar effect on OSDA packing within the zeolite and have an impact on the accessible orientations an OSDA can adopt. ^{29,64} However, our augmented model is able to provide an examination of potential candidates to crystallize CHA or AEI with better resolution than just using the GHIE alone with no additional computational cost.

Conclusion

OSDA size and shape have a strong influence over the final topology crystallized. Here, we demonstrated for CHA and AEI that the GHIE is not a sufficient stand-alone descriptor. In conjunction with a shape-based descriptor, we can augment the GHIE model to provide better predictions for OSDA phase affinities at virtually no additional cost. We also show that our sampling methods are effective at sampling low-energy configurations of OSDA orientations in the zeolite void (except for the inability of OSDAs to hop between low-energy basins in the high-temperature 1-step annealing approach). These new GHIE models can be extended to other frameworks and OSDAs that have similar cavity shapes. The quantification of the overall fitness of the OSDAs in the zeolite voids can also be used to understand how inorganic structure directing agents can be cocaged with the templating molecules.

Supporting Information

Sample VASP and LAMMPS input files for energy evaluations; links to the code used to generate structures as well as final optimized structures and trajectories from the Discrete Sampling and High-Temperature 1-Step Annealing methods; table of OSDA names and phase they experimentally crystallize; orientational landscapes of OSDAs 2-7 and 9-11 from the Discrete Sampling method; orientational landscapes of OSDAs 1-11 from the High-Temperature 1-Step Annealing method; pictorial representations of the low energy structures of OSDAs 1-11 in CHA and AEI; table of OSDAs with GHIE's from the OSDB with computed asymmetry indices.

Acknowledgements

The authors gratefully acknowledge financial support from CBET-DMREF program under award number 1922154. We would like to thank Dr. Vivek Vattipalli for the helpful discussions and input. The computing resources for this work were provided by the Notre Dame Center for Research Computing.

References

- (1) Breck, D. W.; Breck, D. W. Zeolite molecular sieves: structure, chemistry, and use; John Wiley & Sons, 1973.
- (2) Bekkum, H. v.; Jansen, J.; Flanigen, E. Introduction to zeolite science and practice.

 1991,
- (3) Moliner, M.; Rey, F.; Corma, A. Towards the rational design of efficient organic structure-directing agents for zeolite synthesis. *Angew. Chem.*, *Int. Ed.* **2013**, *52*, 13880–13889.

- (4) Pinar, A. B.; Gòmez-Hortigüela, L.; McCusker, L. B.; Perez-Pariente, J. Controlling the aluminum distribution in the zeolite ferrierite via the organic structure directing agent. *Chem. Mater.* **2013**, *25*, 3654–3661.
- (5) Li, C.; Paris, C.; Martínez-Triguero, J.; Boronat, M.; Moliner, M.; Corma, A. Synthesis of reaction-adapted zeolites as methanol-to-olefins catalysts with mimics of reaction intermediates as organic structure-directing agents. *Nat. Catal.* **2018**, *1*, 547–554.
- (6) Dusselier, M.; Davis, M. E. Small-pore zeolites: synthesis and catalysis. Chem. Rev. 2018, 118, 5265–5329.
- (7) Li, J.; Corma, A.; Yu, J. Synthesis of new zeolite structures. *Chem. Soc. Rev.* **2015**, 44, 7112–7127.
- (8) Boal, B. W.; Schmidt, J. E.; Deimund, M. A.; Deem, M. W.; Henling, L. M.; Brand, S. K.; Zones, S. I.; Davis, M. E. Facile synthesis and catalysis of pure-silica and heteroatom LTA. *Chem. Mater.* **2015**, *27*, 7774–7779.
- (9) Schmidt, J. E.; Deimund, M. A.; Xie, D.; Davis, M. E. Synthesis of RTH-type zeolites using a diverse library of imidazolium cations. *Chem. Mater.* **2015**, *27*, 3756–3762.
- (10) Simancas, R.; Dari, D.; Velamazán, N.; Navarro, M. T.; Cantín, A.; Jordá, J. L.; Sastre, G.; Corma, A.; Rey, F. Modular organic structure-directing agents for the synthesis of zeolites. *Science* 2010, 330, 1219–1222.
- (11) Lin, Z. S.; Huang, Y. Tetraalkylammonium salt/alcohol mixtures as deep eutectic solvents for syntheses of high-silica zeolites. *Microporous Mesoporous Mater.* **2016**, *224*, 75–83.
- (12) Yamamoto, K.; Ikeda, T.; Onodera, M.; Muramatsu, A.; Mizukami, F.; Wang, Y.; Gies, H. Synthesis and structure analysis of RUB-50, an LEV-type aluminosilicate zeolite. *Microporous Mesoporous Mater.* 2010, 128, 150–157.

- (13) Miyake, M.; Uehara, H.; Suzuki, H.; Yao, Z.; Matsuda, M.; Sato, M. Syntheses of chromium (III)-doped aluminophosphate-5 molecular sieves from various gels. *Microporous and Mesoporous Mater.* **1999**, *32*, 45–53.
- (14) Gies, H.; Marler, B. The structure-controlling role of organic templates for the synthesis of porosils in the systems SiO2/template/H2O. Zeolites 1992, 12, 42–49.
- (15) Gies, H. Stud Surf Sci Catal; Elsevier, 1994; Vol. 85; pp 295–327.
- (16) Kubota, Y.; Helmkamp, M. M.; Zones, S. I.; Davis, M. E. Properties of organic cations that lead to the structure-direction of high-silica molecular sieves. *Microporous Materials* **1996**, *6*, 213–229.
- (17) Wagner, P.; Nakagawa, Y.; Lee, G. S.; Davis, M. E.; Elomari, S.; Medrud, R. C.; Zones, S. Guest/host relationships in the synthesis of the novel cage-based zeolites SSZ-35, SSZ-36, and SSZ-39. J. Am. Chem. Soc. 2000, 122, 263–273.
- (18) Cundy, C. S.; Cox, P. A. The hydrothermal synthesis of zeolites: Precursors, intermediates and reaction mechanism. *Microporous Mesoporous Mater.* **2005**, *82*, 1–78.
- (19) Nakagawa, Y.; Lee, G.; Harris, T.; Yuen, L.-T.; Zones, S. Guest/host relationships in zeolite synthesis: Ring-substituted piperidines and the remarkable adamantane mimicry by 1-azonio spiro [5.5] undecanes. *Microporous Mesoporous Mater.* **1998**, *22*, 69–85.
- (20) Baerlocher, C.; Gramm, F.; Massüger, L.; McCusker, L. B.; He, Z.; Hovmöller, S.; Zou, X. Structure of the polycrystalline zeolite catalyst IM-5 solved by enhanced charge flipping. Science 2007, 315, 1113–1116.
- (21) Jackowski, A.; Zones, S.; Burton, A. Studies in Surface Science and Catalysis; Elsevier, 2008; Vol. 174; pp 111–116.

- (22) Jackowski, A.; Zones, S. I.; Hwang, S.-J.; Burton, A. W. Diquaternary ammonium compounds in zeolite synthesis: cyclic and polycyclic N-heterocycles connected by methylene chains. J. Am. Chem. Soc. 2009, 131, 1092–1100.
- (23) Asgar Pour, Z.; Sebakhy, K. O. A Review on the Effects of Organic Structure-Directing Agents on the Hydrothermal Synthesis and Physicochemical Properties of Zeolites.

 Chemistry 2022, 4, 431–446.
- (24) Lew, C. M.; Xie, D.; Schmidt, J. E.; Elomari, S.; Davis, T. M.; Zones, S. I. AI-Guided Design and Property Prediction for Zeolites and Nanoporous Materials; John Wiley Sons, Ltd, 2023; Chapter 1, pp 1–32.
- (25) Lewis, D. W.; Willock, D. J.; Catlow, C. R. A.; Thomas, J. M.; Hutchings, G. J. De novo design of structure-directing agents for the synthesis of microporous solids. *Nature* 1996, 382, 604–606.
- (26) Schmidt, J. E.; Deem, M. W.; Lew, C.; Davis, T. M. Computationally-guided synthesis of the 8-ring zeolite AEI. *Top. Catal.* **2015**, *58*, 410–415.
- (27) Burton, A. W.; Lee, G. S.; Zones, S. I. Phase selectivity in the syntheses of cage-based zeolite structures: An investigation of thermodynamic interactions between zeolite hosts and structure directing agents by molecular modeling. *Microporous Mesoporous Mater*. 2006, 90, 129–144.
- (28) Zones, S. I.; Jayanthi, K.; Pascual, J.; Xie, D.; Navrotsky, A. Energetics of the local environment of structure-directing agents influence zeolite synthesis. *Chem. Mater.* **2021**, 33, 2126–2138.
- (29) Muraoka, K.; Chaikittisilp, W.; Okubo, T. Multi-objective de novo molecular design of organic structure-directing agents for zeolites using nature-inspired ant colony optimization. *Chem. Sci.* **2020**, *11*, 8214–8223.

- (30) Leon, S.; Sastre, G. Zeolite phase selectivity using the same organic structure-directing agent in fluoride and hydroxide media. J. Phys. Chem. C 2022, 126, 2078–2087.
- (31) Jensen, Z.; Kwon, S.; Schwalbe-Koda, D.; Paris, C.; Gómez-Bombarelli, R.; Román-Leshkov, Y.; Corma, A.; Moliner, M.; Olivetti, E. A. Discovering relationships between OSDAs and zeolites through data mining and generative neural networks. ACS Cent. Sci 2021, 7, 858–867.
- (32) Schwalbe-Koda, D.; Gómez-Bombarelli, R. Benchmarking binding energy calculations for organic structure-directing agents in pure-silica zeolites. J. Chem. Phys 2021, 154, 174109.
- (33) others,, et al. A priori control of zeolite phase competition and intergrowth with high-throughput simulations. *Science* **2021**, *374*, 308–315.
- (34) Shan, Y.; Shan, W.; Shi, X.; Du, J.; Yu, Y.; He, H. A comparative study of the activity and hydrothermal stability of Al-rich Cu-SSZ-39 and Cu-SSZ-13. *Appl. Catal. B* **2020**, *264*, 118511.
- (35) Martín, N.; Li, Z.; Martínez-Triguero, J.; Yu, J.; Moliner, M.; Corma, A. Nanocrystalline SSZ-39 zeolite as an efficient catalyst for the methanol-to-olefin (MTO) process.

 *ChemComm 2016, 52, 6072–6075.
- (36) DeLuca, M.; Jones, C. B.; Krishna, S. H.; Goswami, A.; Saxena, R.; Li, S.; Prasad, S.; Moini, A.; Schneider, W. F.; Gounder, R. Effects of zeolite framework topology on Cu (I) oxidation and Cu (II) reduction kinetics of NOx selective catalytic reduction with NH3. Chem Catal. 2023,
- (37) Burton, A. W.; Zones, S. I.; Elomari, S. The chemistry of phase selectivity in the synthesis of high-silica zeolites. *Curr Opin Solid State Mater Sci* **2005**, *10*, 211–219.

- (38) Pophale, R.; Daeyaert, F.; Deem, M. W. Computational prediction of chemically synthesizable organic structure directing agents for zeolites. *J. Mater. Chem.* **2013**, *1*, 6750–6760.
- (39) Schwalbe-Koda, D.; Gómez-Bombarelli, R. Supramolecular recognition in crystalline nanocavities through Monte Carlo and Voronoi network algorithms. *J. Phys. Chem. C* **2021**, *125*, 3009–3017.
- (40) Turrina, A.; Cox, P. A. Insights into the Chemistry of Organic Structure-Directing Agents in the Synthesis of Zeolitic Materials; Springer, 2018; pp 75–102.
- (41) Willock, D. J.; Lewis, D. W.; Catlow, C. R. A.; Hutchings, G. J.; Thomas, J. M. Designing templates for the synthesis of microporous solids using de novo molecular design methods. J Mol Catal A Chem 1997, 119, 415–424.
- (42) Devosburchart, E. Studies on Zeolites: Molecular mechanics, framework stability, and crystal growth. Ph.D. thesis, Technische Univ., Delft, 1992.
- (43) Rappé, A. K.; Casewit, C. J.; Colwell, K.; Goddard III, W. A.; Skiff, W. M. UFF, a full periodic table force field for molecular mechanics and molecular dynamics simulations. J. Am. Chem. Soc. 1992, 114, 10024–10035.
- (44) Gálvez-Llompart, M.; Cantín, A.; Rey, F.; Sastre, G. Computational screening of structure directing agents for the synthesis of zeolites. A simplified model. *Z. Kristallogr. Cryst. Mater.* **2019**, *234*, 451–460.
- (45) Mayo, S. L.; Olafson, B. D.; Goddard, W. A. DREIDING: a generic force field for molecular simulations. J. Phys. Chem. 1990, 94, 8897–8909.
- (46) Baerlocher, C.; McCusker, L. Database of Zeolite Structures. http://www.iza-structure.org/databases/, Accessed: 2022-04-08.

- (47) Kresse, G.; Furthmüller, J. Efficient iterative schemes for ab initio total-energy calculations using a plane-wave basis set. *Phys. Rev. B* **1996**, *54*, 11169.
- (48) Blöchl, P. E. Projector Augmented-Wave Method. Phys. Rev. B 1994, 50, 17953.
- (49) Kresse, G.; Joubert, D. From Ultrasoft Pseudopotentials to the Projector Augmented-Wave Method. *Phys. Rev. B* **1999**, *59*, 1758.
- (50) Perdew, J. P.; Burke, K.; Ernzerhof, M. Generalized Gradient Approximation Made Simple. *Phys. Rev. Lett.* **1996**, *77*, 3865.
- (51) Grimme, S.; Ehrlich, S.; Goerigk, L. Effect of the damping function in dispersion corrected density functional theory. *J. Comput. Chem.* **2011**, *32*, 1456–1465.
- (52) Wang, X.; Wang, Y.; Moini, A.; Gounder, R.; Maginn, E. J.; Schneider, W. F. Influence of an N, N, N-Trimethyl-1-adamantyl Ammonium (TMAda+) Structure Directing Agent on Al Distributions and Pair Features in Chabazite Zeolite. Chem. Mater. 2022, 34, 10811–10822.
- (53) Evans, D. J.; Holian, B. L. The Nose–Hoover thermostat. *J. Chem. Phys* **1985**, *83*, 4069–4074, Publisher: American Institute of Physics.
- (54) Thompson, A. P.; Aktulga, H. M.; Berger, R.; Bolintineanu, D. S.; Brown, W. M.; Crozier, P. S.; in't Veld, P. J.; Kohlmeyer, A.; Moore, S. G.; Nguyen, T. D.; et al. LAMMPS-a flexible simulation tool for particle-based materials modeling at the atomic, meso, and continuum scales. Comput Phys Commun 2022, 271, 108171.
- (55) Zones, S. I.; Burton, A. W.; Lee, G. S.; Olmstead, M. M. A study of piperidinium structure-directing agents in the synthesis of silica molecular sieves under fluoride-based conditions. *J. Am. Chem. Soc.* **2007**, *129*, 9066–9079.
- (56) Larsen, A. H.; Mortensen, J. J.; Blomqvist, J.; Castelli, I. E.; Christensen, R.; Dułal, M.; Friis, J.; Groves, M. N.; Hammer, C.; Hargus, C.; et al. The Atomic Simulation Envi-

- ronment—a Python library for working with atoms. J. Condens. Matter Phys. 2017, 29, 273002.
- (57) Li, S.; Gounder, R.; Debellis, A.; Müller, I. B.; Prasad, S.; Moini, A.; Schneider, W. F. Influence of the N, N, N-Trimethyl-1-adamantyl Ammonium Structure-Directing Agent on Al Substitution in SSZ-13 Zeolite. J. Phys. Chem. C 2019, 123, 17454–17458.
- (58) Villaescusa, L. A.; Bull, I.; Wheatley, P. S.; Lightfoot, P.; Morris, R. E. The location of fluoride and organic guests in 'as-made'pure silica zeolites FER and CHA. J. Mater. Chem. 2003, 13, 1978–1982.
- (59) Dusselier, M.; Schmidt, J. E.; Moulton, R.; Haymore, B.; Hellums, M.; Davis, M. E. Influence of organic structure directing agent isomer distribution on the synthesis of SSZ-39. Chem. Mater. 2015, 27, 2695–2702.
- (60) Leon, S.; Sastre, G. Computational screening of structure-directing agents for the synthesis of pure silica ite zeolite. *J. Phys. Chem. Lett.* **2020**, *11*, 6164–6167.
- (61) Todeschini, R.; Consonni, V. *Handbook of molecular descriptors*; John Wiley & Sons, 2008.
- (62) Matamala, A. R. A Box-Model Approach to Molecular Shape. J. Chil. Chem. Soc. **2016**, 61, 3250–3254.
- (63) Nakagawa, Y.; Lee, G. S.; Zones, S. I. Process for preparing zeolites using substituted-piperidinium cations. 2000; US Patent 6,086,848.
- (64) Toby, B. H.; Khosrovani, N.; Dartt, C. B.; Davis, M. E.; Parise, J. B. Structure-directing agents and stacking faults in the CON system: a combined crystallographic and computer simulation study. *Microporous Mesoporous Mater.* **2000**, *39*, 77–89.

Graphical TOC Entry

